PERGAMON

Carbon 40 (2002) 2043–2061

CARBON

Review

Raman spectroscopy on isolated single wall carbon nanotubes ☆

M.S. Dresselhaus[a,b,*], G. Dresselhaus[c], A. Jorio[b,d], A.G. Souza Filho[b,e], R. Saito[f]

[a]*Department of Electrical Engineering and Computer Science, Massachusetts Institute of Technology, Cambridge, MA 02139-4307, USA*

[b]*Department of Physics, Massachusetts Institute of Technology, Cambridge, MA 02139-4307, USA*

[c]*Francis Bitten Magnet Laboratory, Massachusetts Institute of Technology, Cambridge, MA 02139-4307, USA*

[d]*Departamento de Física, Universidade Federal de Minos Grois, Belo Horizonta, MG, 30123-970, Brazil*

[e]*Departamento de Física, Universidade Federal de Ceará, Fortalaga, CE, 60455-760, Brazil*

[f]*Department of Electronic-Engineering, University of Electro-Communications, Tokyo 182-8585, Japan*

Received 16 October 2001; accepted 16 December 2001

Abstract

A review is presented on the resonance Raman spectra from one isolated single wall carbon nanotube. The reasons why it is possible to observe the spectrum from only one nanotube are given and the important structural information that is provided by single nanotube spectroscopy is discussed. Emphasis is given to the new physics revealed by the various phonon features found in the single nanotube spectra and their connection to spectra observed for single wall nanotube bundles. The implications of this work on single wall carbon nanotube research generally are also indicated.

Keywords: Raman spectroscopy; Single wall carbon nanotubes

1. Introduction

Much has been written about the remarkable electronic properties which allow a single wall carbon nanotube (SWNT) one atom in thickness, a few tens of atoms in circumference, and many microns in length, to be either semiconducting or metallic, depending on its diameter and chirality [1,2]. Phonons provide a sensitive probe of the electronic structure through the coupling between electrons and phonons in this one-dimensional system. Furthermore, this coupling gives rise to highly unusual Raman spectra, when the photon involved in the Raman process is in resonance with an electronic state in this highly one-dimensional material. Since the electronic states are highly sensitive to the diameter of the nanotube, the resonance Raman effect is likewise highly sensitive of the nanotube diameter [3]. In some cases, chirality-dependent behavior is also observed.

An important recent breakthrough in carbon nanotube research has been the observation of Raman spectra from just one isolated single wall carbon nanotube (SWNT) [4]. The observation of Raman spectra from just one nanotube is possible because of the very large density of electronic states close to the van Hove singularities of this one-dimensional structure. When the incident or scattered photons are in resonance with an electronic transition between van Hove singularities in the valence and conduction bands, the Raman cross-section becomes very large due to the strong coupling which occurs between the electrons and phonons of the nanotube under these resonance conditions.

This strong resonance condition allows us to obtain large signal enhancement and thus to observe, on the single nanotube level, each feature of the carbon nanotube Raman spectrum that is usually observed in SWNT bundles [3]. The possibility of single nanotube spectroscopy allows us to study the dependence of each of these features on nanotube diameter and chiral angle, as well as to obtain information about the intensity, linewidth, and polarization

☆ American Carbon Society Medal Award Lecture, Lexington, KY, July 2001.

*Corresponding author. Tel.: +1-617-253-6864; fax: +1-617-253-6827.

E-mail address: millie@mgm.mit.edu (M.S. Dresselhaus).

0008-6223/02/$ – see front matter
PII: S0008-6223(02)00066-0

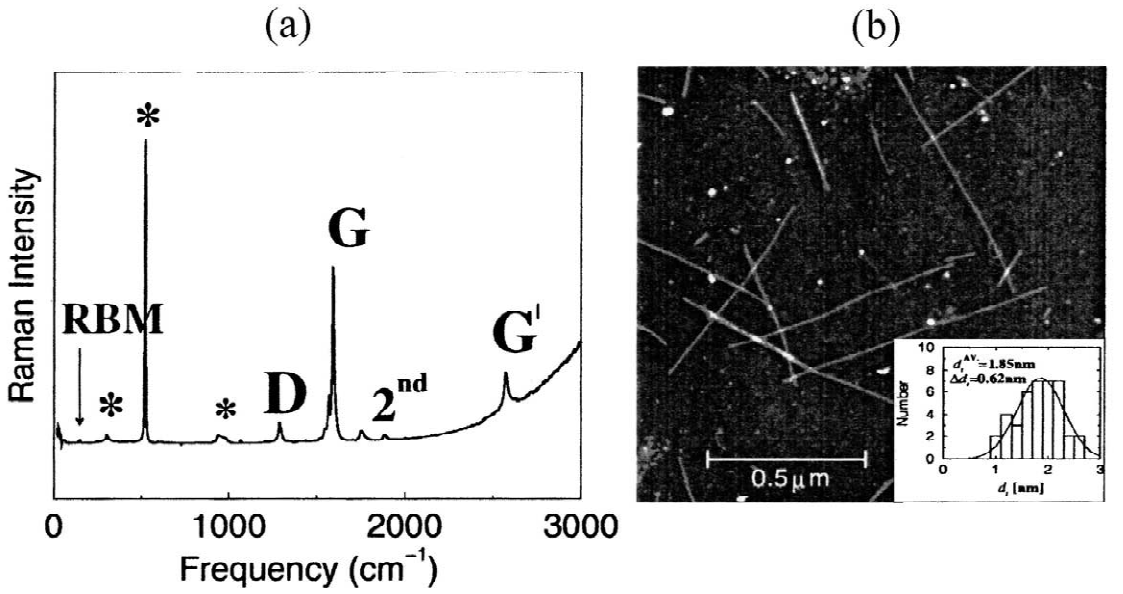

Fig. 1. (a) Raman spectrum from one nanotube taken over a broad frequency range using $E_{laser} = 785$ nm $= 1.58$ eV excitation, and showing the radial breathing mode (RBM), the D-band, the G-band, and the G′-band. Second-order modes are also observed, but are not discussed in this paper. The features marked with '*' at 303, 521 and 963 cm^{-1} are from the Si/SiO_2 substrate [5] and are used for calibration of the nanotube Raman spectrum. (b) AFM image of the sample showing isolated single wall nanotubes grown from the vapor phase [6]. The small particles are iron catalyst particles. The inset shows the diameter distribution of this sample based on AFM observations of 40 SWNTs [4].

properties of each feature, its dependence on laser excitation energy, and finally the connection between spectra at the single nanotube level to Raman spectra normally observed from single wall carbon nanotube bundles. A survey of present knowledge of each of these features is one of the goals of this review article.

Of particular interest are the many new physical phenomena that have been discovered through observation of the Raman spectrum from one isolated nanotube, and a survey of these new phenomena is the other main goal of this review. The most important of these is the use of resonance Raman spectroscopy to yield the geometrical structure of one isolated individual SWNT. The background which explains how this is possible is presented in this introductory section. The following sections summarize present knowledge about the most important features in the single nanotube Raman spectra shown in Fig. 1a: the radial breathing mode (RBM), the tangential G-band (derived from the graphite-like in-plane mode), the disorder-induced D-band, and its second-order harmonic (the G′-band). In connection with each Raman feature, the new physics that has been found by study of that particular feature is discussed under appropriate sub-headings (see Table 1).

The isolated SWNTs used in these single nanotube Raman experiments were prepared by a chemical vapor deposition method on a Si substrate containing nanometer size iron catalyst particles. Since the substrate is oxidized to form a thin SiO_2 surface coating, no significant charge transfer is expected between the SWNTs and the substrate. Since the nanotubes nucleate and grow from well isolated catalyst particles, nanotube bundles are not formed. Fig. 1b shows an atomic force microscopy (AFM) image of a sample with a high SWNT concentration (6 ± 3 SWNTs per μm^2) for easy visualization. Most nanotubes are individual SWNTs, but a few of them are entangled with

Table 1
Vibrational modes observed for Raman scattering in SWNTs

Notation	Frequency (cm^{-1})	Symmetry	Type of mode
RBM[a]	$248/d_t$	A	In phase radial displacements
D-band	~1350	–	Defect-induced, dispersive
G-band	1550–1605	A, E_1, E_2	Graphite-related optical mode[b]
G′-band	~2700	–	Overtone of D-band, highly dispersive

[a] RBM denotes radial breathing mode.
[b] The related 2D graphite mode has E_{2g} symmetry. In 3D graphite, the corresponding mode is denoted by E_{2g_2}

each other, showing a 'Y' shape or a tube crossing. The inset to Fig. 1b shows the wide diameter distribution of the SWNT samples ($\sim 1 < d_t < 3$ nm) typically used in these studies. Resonance Raman spectra in the 100 to ~3000 cm^{-1} spectral range from these individual isolated SWNTs are taken with a readily available Raman microprobe instrument, such as a Renishaw Raman Microprobe (1-μm laser spot), using ~1 mW laser power, and laser excitation, such as $E_{laser} = 514.5$ nm $= 2.41$ eV. The Raman spectrum shown in Fig. 1a was taken with a Kaiser micro-Raman spectrograph operating at a laser excitation energy of 1.58 eV. Relatively high laser powers can be used to probe isolated SWNTs because of their unusually high thermal conductivity [7], excellent high temperature stability, and their good thermal contact to the substrate. Although SWNTs can withstand high incident power levels (~30 mW on 1 μm^2) without damage, most spectra are taken with low power levels (1–10 mW).

Because of the trigonal warping effect shown in Fig. 2b, there is a weak dependence of the electronic energy levels of single wall carbon nanotubes (SWNTs) on chiral angle, as well as a much stronger dependence on nanotube diameter d_t, which determines the number of carbon atoms in the circular cross-section of the nanotube shell, one atom in thickness [2]. The structure of each nanotube is uniquely described by two integers (n, m), which refer to the number of $\vec{a}_1$ and $\vec{a}_2$ unit vectors of the graphene lattice that are contained in the chiral vector, $\vec{C}_h = n\vec{a}_1 + m\vec{a}_2$, that spans the circumference of each nanotube [2]. From the (n, m) indices, one can calculate the nanotube diameter d_t, the chiral angle θ, the electronic energy bands and the density of electronic states [2,8], as well as the energies of the interband transitions $E_{ii}(n, m)$ between the van Hove singularities in the valence and conduction band density of states shown in Figs. 2a and 3 and summarized in Table 2.

The weak dependence of the electronic energy bands of SWNTs on chiral angle relates to the 3-fold symmetry of the electronic dispersion relations about the K-point of the 2D graphene Brillouin zone (see Fig. 2b), where the graphene valence and conduction bands are degenerate, forming a zero band gap semiconductor for a 2D graphene sheet (a single basal plane layer of the graphite lattice) [2]. Away from the K-point, the graphene electronic energy bands exhibit a trigonal warping effect [11–14], as shown in Fig. 2b, and this trigonal warping is responsible for the unique energy bands for the conduction and valence bands for each (n, m) SWNT, when the energy bands of the graphene lattice are zone folded to form the energy bands of the SWNTs [11]. The chirality dependence of the van Hove singularities [11,15] in the 1D electronic density of states (DOS) of the conduction band (where the energy is measured relative to the Fermi energy) are shown in Fig. 3 for several *metallic* (n, m) nanotubes, all having about the same diameter d_t (from 1.31 to 1.43 nm), but having different chiral angles: $\theta = 0°$, 8.9°, 14.7°, 20.2°, 24.8°, and

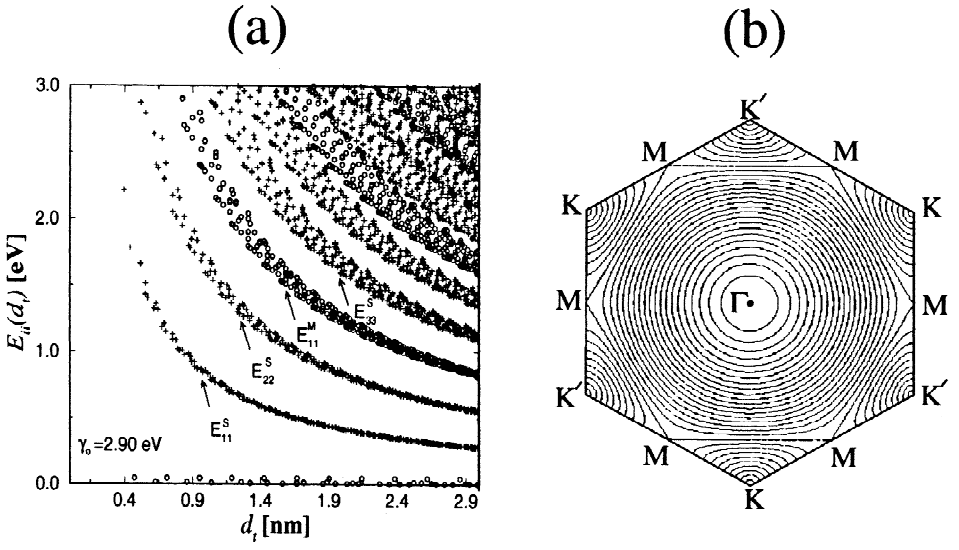

Fig. 2. (a) Calculated [9] energy separations $E_{ii}(d_t)$ between van Hove singularities i in the 1D electronic density of states of the conduction and valence bands for all (n, m) values versus nanotube diameter $0.4 < d_t < 3.0$ nm, using a value for the carbon–carbon energy overlap integral of $\gamma_0 = 2.9$ eV and a nearest neighbor carbon–carbon distance $a_{C-C} = 1.42$ Å [10,11]. Semiconducting (S) and metallic (M) nanotubes are indicated by crosses and open circles, respectively. The index i in the interband transitions E_{ii} denotes the transition between the van Hove singularities, with $i = 1$ being closest to the Fermi level. (b) Plot of the 2D equi-energy contours of graphite, showing trigonal warping effects in the contours, as we move from the K-point in the K−Γ or K−M directions. The equi-energy contours are circles near the K-point and near the center of the Brillouin zone. But near the zone boundary, the contours are straight lines which connect the nearest M-points [11,12].

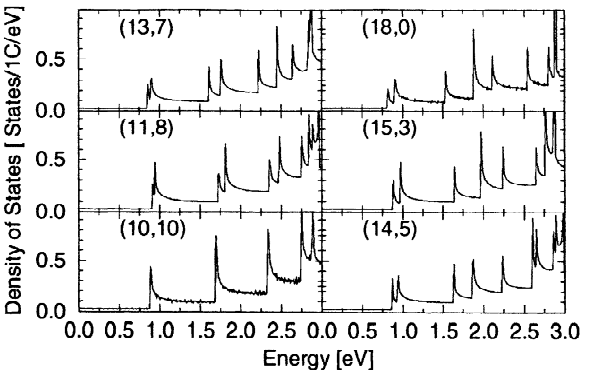

Fig. 3. The 1D electronic density of states versus energy (measured from the Fermi level) for several metallic nanotubes of approximately the same diameter, showing the effect of chirality on the van Hove singularities: (10, 10) (armchair), (11, 8), (13, 7), (14, 5), (15, 3) and (18, 0) (zigzag). Only the densities of states for the conduction π^*-band are shown; the mirror image of these plots gives the electronic density of states for the valence π-band [15] within the tight binding approximation, and assuming the overlap integral to be $s=0$ [2].

30.0° for nanotubes (18, 0), (15, 3), (14, 5), (13, 7), (11, 8), and (10, 10), respectively. The plot shows that as the chiral angle is varied from the armchair nanotube (10, 10) ($\theta=30°$) to the zigzag nanotube (18, 0) ($\theta=0°$), a splitting develops in all of the singularities in the DOS, and this splitting increases with decreasing chiral angle, giving rise to a *unique* set of singularities E_{ii} for each (n, m) value.

This trigonal warping effect consequently causes a spread of the interband energies $E_{ii}(d_t)$ between the singularities in the joint density of states (JDOS) for nanotubes with the same diameter d_t, as shown in Fig. 2a. Here the integer i denotes the singularities in the JDOS as the energy relative to the Fermi level E_F increases. Thus each nanotube (n, m) has a unique set of interband energies E_{ii} denoting the energy differences between the ith van Hove singularities in the conduction and valence bands. And, conversely, if one interband energy E_{ii} and a nanotube diameter are specified, then its corresponding unique (n, m) indices can be identified.

It is well established [2] that the (n, m) indices are crucial to the nanotube electronic structure. Specifically, SWNTs for which $|n-m|=3q$ are metallic and those for

Table 2
Parameters for carbon nanotubes[a]

Symbol	Name	Formula	Value
a	Length of unit vector	$a=\sqrt{3}a_{C-C}=2.46$ Å,	$a_{C-C}=1.42$ Å
$\mathbf{a}_1$, $\mathbf{a}_2$	Unit vectors	$\left(\frac{\sqrt{3}}{2}, \frac{1}{2}\right)a$, $\left(\frac{\sqrt{3}}{2}, -\frac{1}{2}\right)a$	x, y coordinates
$\mathbf{C}_h$	Chiral vector	$\mathbf{C}_h=n\mathbf{a}_1+m\mathbf{a}_2\equiv(n, m)$	$(0\le\|m\|\le n)$
L	Length of $\mathbf{C}_h$	$L=\|\mathbf{C}_h\|=a\sqrt{n^2+m^2+nm}$	
d_t	Diameter	$d_t=L/\pi$	
θ	Chiral angle	$\sin\theta=\frac{\sqrt{3}m}{2\sqrt{n^2+m^2+nm}}$	$0\le\|\theta\|\le\frac{\pi}{6}$
		$\cos\theta=\frac{2n+m}{2\sqrt{n^2+m^2+nm}}$,	$\tan\theta=\frac{\sqrt{3}m}{2n+m}$
d	gcd(n, m)[b]		
d_R	gcd($2n+m$, $2m+n$)[b]	$d_R=\begin{cases}d & \text{if } (n-m) \text{ is not a multiple of } 3d\\ 3d & \text{if } (n-m) \text{ is a multiple of } 3d\end{cases}$	
$\mathbf{T}$	Translational vector	$\mathbf{T}=t_1\mathbf{a}_1+t_2\mathbf{a}_2\equiv(t_1, t_2)$	gcd(t_1, t_2)=1[b]
		$t_1=\frac{2m+n}{d_R}$, $t_2=-\frac{2n+m}{d_R}$	
T	Length of $\mathbf{T}$	$T=\|\mathbf{T}\|=\frac{\sqrt{3}L}{d_R}$	
N	Number of hexagons in the nanotube unit cell	$N=\frac{2(n^2+m^2+nm)}{d_R}$	

[a] In this table n, m are integers and d, d_R, t_1, t_2 and N are integer functions of these integers.
[b] gcd(n, m) denotes the greatest common divisor of the two integers n and m.

which $|n-m| = 3q \pm 1$ are semiconducting, where q is an integer [1,2]. Nevertheless, it has proven difficult to measure (n, m) experimentally and then to carry out property measurements on the same SWNT. We explain in Section 2 how the resonance Raman spectra from one isolated nanotube can conveniently provide this information. As stated above, every possible nanotube denoted by (n, m) has a distinct electronic and vibrational spectrum, so that there is a one-to-one relation between (n, m) and the singularities in the 1D joint electronic density of states [2]. In the resonant Raman effect, a large enhancement in the Raman signal occurs when the incident or scattered photon is in resonance with a singularity in the 1D joint density of states (JDOS) of the SWNT.

What is special about the resonance Raman effect in *isolated* SWNTs is the structural information that is provided by the single nanotube spectra, as discussed in Section 2. Normally the resonance Raman effect just gives spectral information about phonons, electrons, and the electron–phonon interaction, but not structural information directly. But in the resonance Raman process for SWNTs, every (n, m) nanotube is in resonance with a unique interband energy $E_{ii}(n, m)$, as shown in Fig. 2a, so that for the case of this particular 1D system, resonant Raman spectra can also yield structural information through identification of the (n, m) indices for isolated SWNTs. Once (n, m) is known from measurements made on the radial breathing mode feature, Raman studies on isolated carbon nanotubes can be carried out to understand in detail the dependence of all the features shown in the spectrum of Fig. 1a on diameter d_t, chiral angle θ, laser excitation energy E_{laser}, and other parameters. From such knowledge, the spectrum of SWNT bundles can be explained, and by comparison to the spectra measured on SWNT bundles, the effect of nanotube–nanotube interactions can be deduced.

In addition, resonance Raman studies on SWNTs show many new phenomena not yet observed in other physical systems [16–18], and much activity is now in progress in this research area. Resonance Raman characterization of the (n, m) indices for one nanotube is important for future scientific studies of SWNTs, insofar as many physical properties, such as transport, optical, mechanical, and other properties, that depend sensitively on the (n, m) indices [2], can now be studied systematically at the single nanotube level. The (n, m) characterization provided by resonance Raman spectroscopy [4] is a general, rapid (~1 min per spectrum), nondestructive technique that operates at ambient temperature (~300 K) and pressure conditions, and uses readily-available Raman characterization instrumentation. By using well established lithographic marking techniques on an isolated SWNT sample, it is possible to always return to the same nanotube on the oxidized silicon substrate, thereby allowing systematic physical property measurements to be carried out on structurally characterized isolated nanotubes. Such systematic studies will allow detailed comparisons to be made between experiment and theory for many physical properties, since calculations of the physical properties of SWNTs as a function of nanotube diameter and chirality are usually expressed in terms of their (n, m) values.

2. Radial breathing mode

In Section 2.1, we discuss our present knowledge of the characteristic properties of the radial breathing mode (RBM) for single nanotube Raman spectroscopy [3], and in Section 2.2, we discuss how the RBM is used to determine the (n, m) indices. The spectral profile of the JDOS, which relates closely to the resonant enhancement that is possible in single nanotube spectroscopy, is discussed in Section 2.3.

2.1. Characteristics of the radial breathing mode

Fig. 4 shows three Raman spectra in the radial breathing mode spectra region taken for three different isolated SWNTs, each within a different light spot, about 1 μm in diameter, on a sample of isolated SWNTs, such as the one shown in Fig. 1b.

Since the radial breathing mode frequency, ω_{RBM}, depends linearly on the reciprocal nanotube diameter d_t [3], each (n, m) nanotube in a sample with a wide diameter distribution, such as in Fig. 1b, will have a different RBM spectrum. By placing the isolated carbon nanotubes on a slightly oxidized silicon substrate, it is possible to also

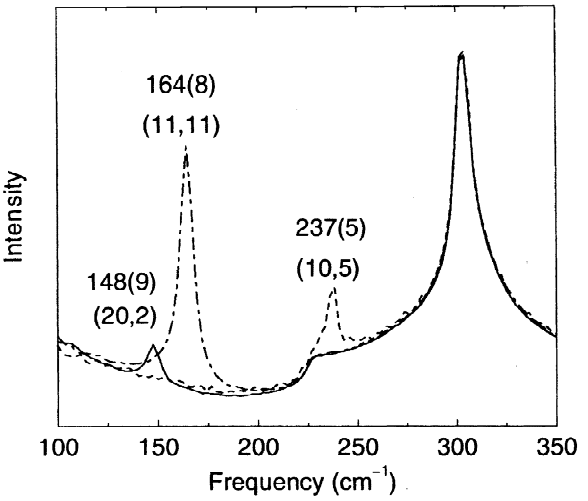

Fig. 4. The superposition of three Raman spectra (solid, dashed, and dash–dotted curves) come from three different spots on the Si substrate, showing the presence of only one resonant nanotube and one RBM frequency for each of the three laser spots. The RBM frequencies (linewidths) and the (n, m) assignments for each resonant SWNT are displayed. The 303-cm^{-1} feature comes from the Si substrate and is used for calibration purposes [4].

obtain Raman spectra from the silicon substrate, and these Si Raman lines are used for accurate calibration of the frequency and of the scattering intensity of the Raman spectra for the individual carbon nanotubes. Since the lineshape of the RBM feature for a single nanotube is a simple Lorentzian line with a linewidth (FWHM) of 4–10 cm^{-1} at room temperature the peak frequency can in most cases be determined to ~1 cm^{-1}. Fig. 4 shows that under favorable resonance Raman conditions, the RBM intensity from only one nanotube is comparable to that of the silicon spectral features from the quasi-3D Si film substrate, because of the large 1D resonance Raman enhancement effect in isolated nanotubes.

The frequency of the RBM, as stated before, varies as $1/d_t$

$$\omega_{\mathrm{RBM}} = \alpha/d_t, \tag{1}$$

and for the Si/SiO_2 substrate α is experimentally found to be 248 cm^{-1} nm for isolated SWNTs. Furthermore, ω_{RBM} is independent of chiral angle θ, as has been shown by both force constant [19] and ab initio calculations [20,21]. At a fixed E_{laser} value, the RBM linewidth is found to increase with increasing nanotube diameter [16] and as the energy difference $|E_{\mathrm{laser}} - E_{ii}|$ between E_{laser} and the resonant interband energy E_{ii} increases. The smallest linewidths are, as expected, obtained under fully resonant conditions where $E_{\mathrm{laser}} = E_{ii}$. Although it is clear from inspection that the intensity of the RBM feature depends on E_{laser}, on whether a nanotube is semiconducting or metallic, and on extrinsic factors such as the length of the nanotube, the alignment of the nanotube with the laser optical electric field, no detailed studies of these properties have yet been made, nor has the intensity dependence on d_t and θ been investigated in detail.

2.2. Determination of (n, m) indices

The determination of (n, m) by resonance Raman scattering depends primarily on the determination of E_{ii} using the unique relation between E_{ii} and (n, m) shown in Fig. 2a, since d_t is found directly from $\omega_{\mathrm{RBM}} = 248/d_t$. The determination of E_{ii} is most conveniently carried out by measurement of the radial breathing mode feature, though other features (such as the G-band, D-band and G′-band) in the resonance Raman spectrum are often used to confirm the (n, m) assignment made from analysis of the RBM spectrum. If a tunable laser were available to be tuned to E_{ii} (which could be detected as the E_{laser} value where the maximum intensity in the Raman spectrum occurs), then a simple measurement of ω_{RBM} (yielding d_t) to identify the index i in E_{ii} (see Fig. 2a) would be sufficient to determine (n, m). In practice, such a tunable laser system has thus far only been applied to single nanotube Raman spectroscopy studies over a small energy range (~0.15 eV) [22], as described in Section 2.3.

Nevertheless, an (n, m) determination can in most cases be made if a nanotube is within the resonant window of a single available laser excitation line, which in practice is satisfied for E_{laser} within $\sim\pm 0.1$ eV of an interband transition for that nanotube. From the measured ω_{RBM} and use of Eq. (1), the nanotube diameter d_t is found, which determines the i index in E_{ii} from Fig. 2a. In many cases there is only one (n, m) value that has both a diameter close to the measured d_t value, determined from the ω_{RBM} measurement, and is also within the resonant window of E_{laser}, as shown in Table 3. For illustrative purposes, this table lists the nanotubes in resonance with E_{11}^{M} and with E_{22}^{S} within the resonant window of $E_{\mathrm{laser}} = 1.58$ eV, where the superscript in E_{11}^{M} distinguishes between metallic (M) and semiconducting (S) nanotubes, and the subscript $ii = 11$ denotes the lowest energy interband transition in the joint density of states (JDOS). We note that for each metallic nanotube (other than armchair nanotubes which are all metallic), there are two resonances corresponding to E_{11}^{M} in the joint density of states [11]. In Table 3 are listed the various (n, m) nanotubes that were identified in the sample shown in Fig. 1b to be in resonance with the E_{11}^{M} and the E_{22}^{S} interband transitions. The table shows their measured ω_{RBM} values and their identified (n, m) indices, as well as their predicted ω_{RBM} and E_{11}^{M} and E_{22}^{S} values [4]. The good agreement achieved between the predicted and observed ω_{RBM} and E_{ii} values using in Eq. (1) and $\gamma_0 = 2.9$ eV for this type of sample confirms the validity of the (n, m) assignments. Other features in the single nanotube spectra (see Fig. 1a) provide additional confirmation of the (n, m) assignments, as discussed elsewhere in this review article.

Returning now to Fig. 4, two of the three spectra, namely those with $\omega_{\mathrm{RBM}} = 148$ and 164 cm^{-1} come from a resonance of $E_{\mathrm{laser}} = 1.58$ eV with E_{11}^{M}, and the third $\omega_{\mathrm{RBM}} = 237$ cm^{-1} spectrum is associated with a resonance with E_{22}^{S}. In each case, the (n, m) values obtained by this method are given in Fig. 4 and are also listed in Table 3.

In cases where two nanotubes have radial breathing mode frequencies within ~1 cm^{-1} of each other, a more accurate and more direct method to determine the (n, m) indices should be used [23]. One method that determines E_{ii} directly requires measurement of both the Stokes and anti-Stokes radial breathing mode spectra [23,24]. In this case, ω_{RBM} is once again used to determine d_t and to designate the transition branch i in E_{ii} (see Fig. 2a). The ratio of the anti-Stokes to Stokes intensities for the radial breathing mode for a given resonant nanotube can then be used to sensitively (to 10 meV) determine the energy E_{ii} of the resonant van Hove singularity in the joint density of states [23], thereby providing a unique identification of the (n, m) indices. When the anti-Stokes to Stokes intensities are exactly equal to the Boltzmann factor at the measurement temperature for ω_{RBM}, then E_{laser} is in exact resonance with E_{ii}, resulting in very large intensities for all of the features in the Raman spectra, as shown in Fig. 5 for a

Table 3
Possible (n, m) and their calculated ω_{RBM} and E_{ii} values in the resonant window $1.48 \leq E_{ii} \leq 1.68$ eV for $E_{laser} = 1.58$ eV, where $E_{ii} = E_{11}^{M}$ for metallic SWNTs and $E_{ii} = E_{22}^{S}$ for semiconducting SWNTs (see Fig. 2a)

(n, m)	d_t (nm)	θ (°)	ω_{RBM} (cm^{-1})[a]		E_{11}^{M}[b] (eV)	
			(calc.)	(exp.)		
(18, 6)	1.72	13.9	144.4	144(2)	1.49	1.40
(19, 4)	1.69	9.4	146.8	–	1.53	1.42
(20, 2)	1.67	4.7	148.3	–	**1.55**	1.42
(21, 0)	1.67	0.0	148.8	**148**(5)[c]	**1.56**	1.43
(15, 9)	1.67	21.8	148.8	–	1.51	1.46
(12,12)	1.65	30.0	150.3	**151**(3)	1.50	
(16, 7)	1.62	17.3	153.0	**154**(5)	**1.57**	1.49
(17, 5)	1.59	12.5	156.4	**156**(6)	**1.62**	1.51
(13, 10)	1.59	25.7	156.4	**156**(1)	**1.58**	**1.55**
(18, 3)	1.56	7.6	158.8	158(1)	1.66	1.52
(19, 1)	1.55	2.5	160.0	**160**(3)	1.68	**1.54**
(14, 8)	1.53	21.1	162.0	161(1)	1.65	**1.58**
(11, 11)	1.51	30.0	164.0	**164**(1)	**1.63**	
(15, 6)	1.49	16.1	166.7	**165**(1)	1.72	**1.62**
(16, 4)	1.46	10.9	170.4	169(1)	1.79	1.64
(17, 2)	1.44	5.5	172.7	174(1)	1.81	1.65
(18, 0)	1.43	0.0	173.5	176(1)	1.83	1.65
					E_{22}^{S}[d]	
(14, 1)	1.15	3.4	215.1	210(1)	1.50	
(10, 6)	1.11	21.8	223.1	–	1.51	
(9, 7)	1.10	25.9	224.9	–	1.48	
(11, 4)	1.07	14.9	232.2	229(1)	**1.60**	
(10, 5)	1.05	19.1	236.1	237(2)	**1.54**	
(12,2)	1.04	7.6	238.2	–	1.66	
(8,7)	1.03	27.8	240.3	239(2)	**1.61**	
(11,3)	1.01	11.7	244.7	–	**1.57**	

Resonance with E_{33}^{S} and E_{44}^{S} is also possible under these conditions, but these resonant SWNTs are not listed in this table. The experimentally observed ω_{RBM} values are also listed, along with the number of times (between parentheses) each (n, m) was found for a particular experiment on a particular sample [4]

[a] Bold face indicates those ω_{RBM} observed to have a relatively large intensity.

[b] Two E_{11}^{M} values are given for each crystalline chiral (n, m) SWNT because of the trigonal warping effect, but armchair (n, m) nanotubes have only one E_{ii} value. Bold face indicates E_{ii} values predicted to have large intensities.

[c] In this particular experiment there was an ambiguity between (20,2) and (21,0) in the (n, m) assignment.

[d] Each semiconducting nanotube, such as those in resonance with E_{22}^{S}, has only one E_{22}^{S} value.

(14, 8) nanotube in resonance with E_{laser}. For this situation, the resonance is so strong that even the anti-Stokes feature for the G-band at about 1580 cm^{-1} can be clearly seen (see inset to Fig. 5c).

In practice, the (n, m) index characterization for isolated nanotubes can be simply carried out by using a single laser excitation energy E_{laser} when the nanotube is in strong resonance with E_{laser}. If the (n, m) values of every nanotube in the sample must be found, then a tunable laser is needed to provide a resonant excitation energy for each nanotube, so that a complete (n, m) Raman characterization can be carried out for each SWNT.

2.3. Spectral profile of the joint density of states

Measurement of the spectral profile of the 1D joint density of states (JDOS) for a single wall carbon nanotube near a van Hove singularity gives direct evidence for the sharp singularities in the JDOS, thereby showing how it is possible to get sufficient intensity to observe a Raman spectrum from just one nanotube [22]. To determine the JDOS spectral profile, the (n, m) value of the nanotube is first determined reliably by measuring the resonant Stokes and anti-Stokes Raman spectrum for this nanotube. The spectral profile of the JDOS is determined by using many laser energies over a narrow energy range, as is provided by a tunable laser. The experiments are carried out on a sample containing lithographic markers, so that as the laser energy is tuned, the microscope focus can always be brought to the same nanotube. The RBM integrated intensity $I(E_{laser})$ is a function of E_{laser} and can be evaluated from the joint density of states $g(E)$ according to the theory for incoherent light scattering

$$I(E_{laser}) = \int \left| M \frac{g(E)}{(E_{laser} - E - i\Gamma_r)(E_{laser} \pm E_{ph} - E - i\Gamma_r)} \right|^2 dE \quad (2)$$

in which the first and second factors in the denominator, respectively, describe the resonance effect with the incident and scattered light, where the $+(-)$ applies to the anti-Stokes (Stokes) process for a phonon of energy E_{ph}, while Γ_r gives the inverse lifetime for the resonant scattering process, and the matrix element for the scattering process $M = M_i M_{ep} M_s$ is considered to be independent of E in the small energy range of the resonance. Here M_i, M_s and M_{ep} are, respectively, the matrix elements for the electron-radiation absorption, the electron-radiation emission, and the electron–phonon interaction, while the JDOS profile $g(E)$ can be approximated by

$$g(E) = Re\left[\sum_i \frac{a_{C-C} E}{d_t \gamma_0 \sqrt{[(E - E_{ii} - i\Gamma_J)(E + E_{ii} + i\Gamma_J)}} \right] \quad (3)$$

where a_{C-C} is the nearest-neighbor distance between carbon atoms, γ_0 is the tight binding energy overlap integral, and Γ_J is introduced as a measure of the effect of the finite nanotube size and the national lifeline on the width of the JDOS singularity for the E_{ii} electronic transition. The sum over i takes into account the different van Hove singularities of one SWNT (see Fig. 3).

Experimentally, a fit of the data points in Fig. 6 determines the values of the fitting parameters in Eqs. (2)

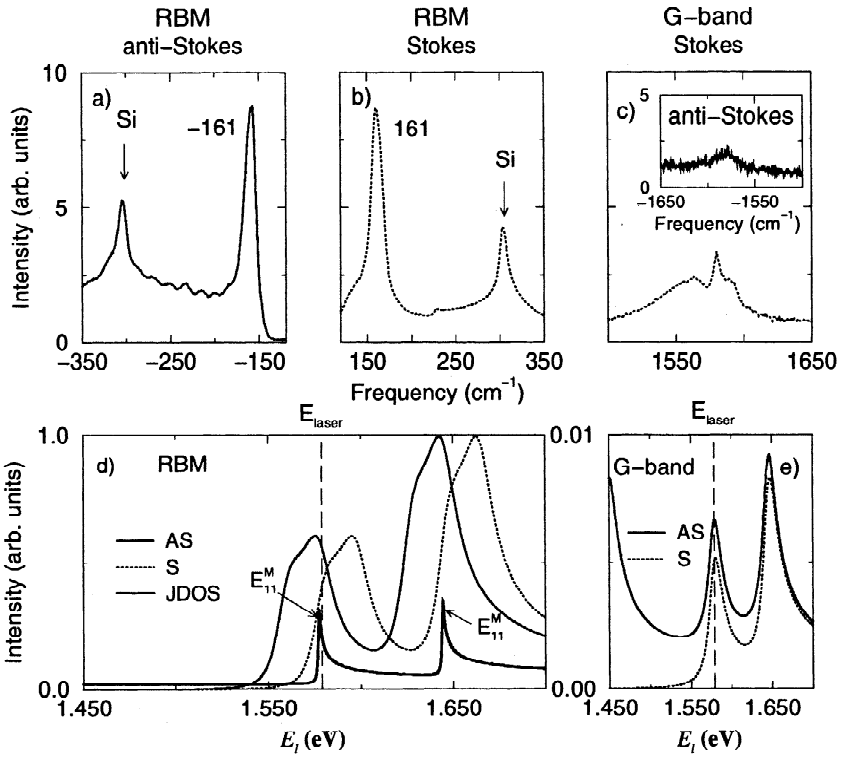

Fig. 5. (a–c) Resonance anti-Stokes and Stokes spectra for a (14, 8) metallic SWNT on a Si/SiO_2 substrate using 1.579 eV (785 nm) laser excitation. The peak at 303 cm^{-1} comes from the Si substrate and is used for calibration purposes, while ω_{RBM} for the tube is 161 cm^{-1}. The anti-Stokes spectra are shown after correcting for the Boltzmann factor $\exp(E_{ph}/kT)$ to permit easy comparison to be made between the Stokes and anti-Stokes spectra. (d) Predicted joint density of states (heavy line) and resonant windows for the RBM mode in the anti-Stokes (solid line) and Stokes (dotted line) processes for the (14, 8) SWNT. (e) Predicted resonant window for the G-band in the region where the resonance is with the incident photon. The van Hove singularity at 1.580 eV is a very strong resonance, while the singularity at 1.642 eV is too far from E_{laser} (vertical dashed lines) for the incident photon and also too far from $E_{laser} \pm E_G$ for the scattered photon to contribute significantly to the G-band spectra shown. The tail in (e) for the anti-Stokes intensity I_{AS} is due to the resonance with the scattered photon ($E_{11}^M - E_G = 1.445$ eV) which comes from the van Hove singularity at 1.642 eV, and $E_G = 0.197$ eV is associated with the G-band phonon [23] (see Section 3.2).

and (3), showing that Γ_r is most sensitive to determining the FWHM linewidth of the spectral features, but that the very small value of Γ_J (~0.5 meV) gives rise to the very strong intensity enhancement (>1000) associated with the sharp 1D van Hove singularities in the joint density of states $g(E)$. Once the parameters in Eqs. (2) and (3) are found, the spectral profile of the JDOS can be plotted, as in the inset to Fig. 6, where $g(E)$ is seen to be highly asymmetric and to have very sharp singularities, with a linewidth of less than 1 meV. Measurements of the Stokes and anti-Stokes spectra over the whole resonant window of the nanotube yield the E_{ii} value more accurately (to 3 meV) than when using a single laser line (~10 meV accuracy). Many physical properties, such as transport, optical, and mechanical properties, are very sensitive to the spectral profile of the electronic density of states, but the profile is difficult to measure directly, because probes, such as scanning tunneling microscopy tips [14], interact too strongly with the nanotube, thereby broadening the van Hove singularities (from less than 1 meV to more than 10 meV), and consequently also broadening the density of states that is probed by scanning probe methods [14].

3. G-band

3.1. Introduction

The G-band in carbon nanotubes occurring in the 1500–1605-cm^{-1} range is basically derived from the Raman-allowed optical mode E_{2g} of 2D graphite by two zone folding the 2D graphene Brillouin zone into the 1D nanotube Brillouin zone, noting that only modes with A, E_1, and E_2 symmetry are Raman active for single wall carbon nanotubes [2,3]. The G-band is thus an intrinsic feature of carbon nanotubes that is closely related to

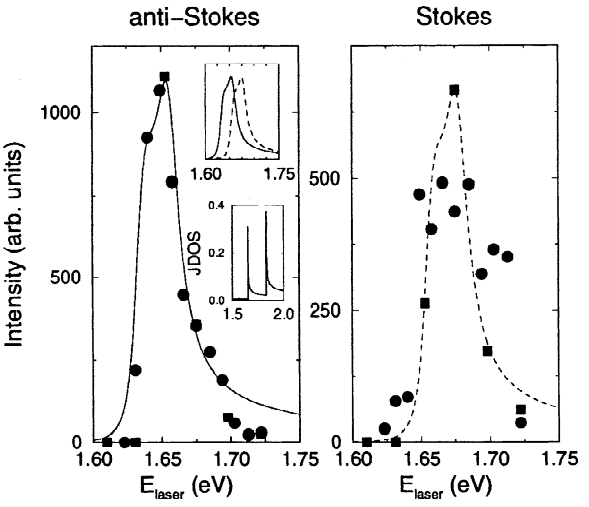

Fig. 6. Raman intensity versus laser excitation energy E_{laser} for the radial breathing mode $\omega_{RBM}=173.6\ cm^{-1}$ peak in the Stokes and anti-Stokes Raman processes of an isolated (18, 0) SWNT, where the anti-Stokes intensity is normalized by $\exp(\hbar\omega_{RBM}/k_BT)$ to facilitate comparisons with the Stokes profile. Circles and squares indicate two different E_{laser} data sets taken on the same SWNT sample. The line curves indicate the resonant Raman windows predicted from Eqs. (2) and (3), with $E_{ii}=1.655$ eV, $\Gamma_r=8$ meV, and $\Gamma_j=0.5$ meV. The upper inset compares the theoretically predicted Stokes and anti-Stokes resonant windows. The lower inset plots the JDOS profile for one isolated (18, 0) SWNT with $\Gamma_j=0.5$ meV for the two lowest energy van Hove singularities.

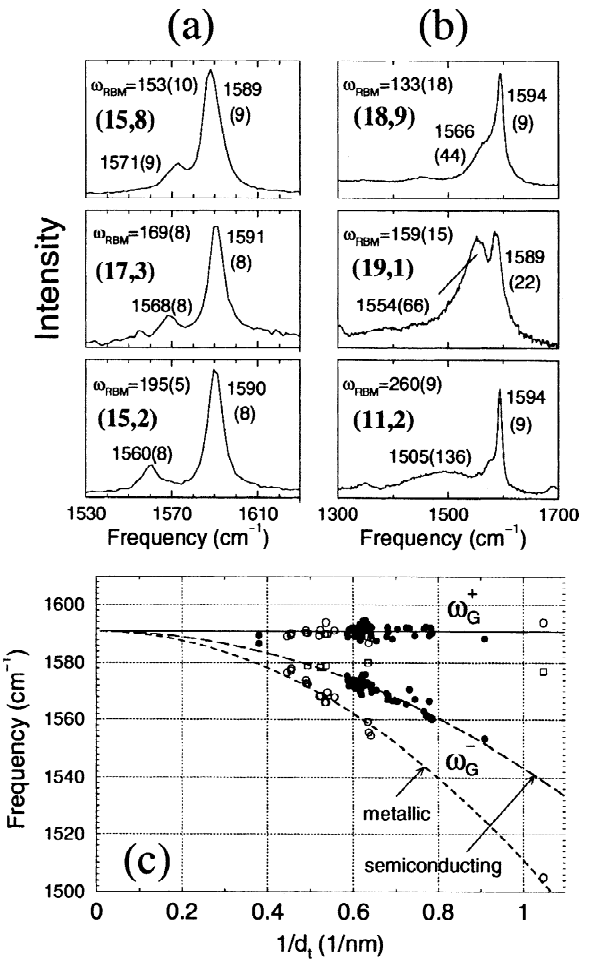

Fig. 7. (a,b) Profiles of the G-band spectra for three semiconducting (a) and three metallic (b) nanotubes whose (n, m) indices are determined by analysis of their RBM spectra. The frequencies for ω_G^+ and ω_G^- are indicated for each nanotube along with the corresponding linewidths in parentheses. (c) Dependence on reciprocal nanotube diameter $1/d_t$ of ω_G^+ and ω_G^- for both semiconducting nanotubes (solid circles) and metallic nanotubes (open circles). The open squares indicate that a peak near ~1580 cm^{-1} is sometimes observed in the Raman spectra for metallic SWNTs [16].

vibrations in all sp^2 carbon materials. The most important aspect of the G-band is the characteristic Raman lineshape (see Fig. 7) which differs in accordance with whether the nanotube is semiconducting or metallic, an intrinsic property of the nanotubes, allowing one to readily distinguish between metallic and semiconducting nanotubes. As in other sp^2 carbons, the G-band in SWNTs is not dispersive and its frequency is not sensitive to E_{laser}. This property helps to distinguish features in the harmonics and combination modes that are associated with the non-dispersive G-band, from those associated with the highly dispersive D-band and G′-band features discussed in Section 4. In Section 3.2 we briefly summarize some of the most important properties of the G-band spectra, while in Sections 3.3–3.5, several important new physical concepts that were discovered through study of the G-band spectra in isolated SWNTs are reviewed.

3.2. General G-band properties

The most dramatic features of the G-band spectra are the characteristic differences between the G-band spectra for metallic and semiconducting nanotubes, shown in Fig. 7. Isolated semiconducting nanotubes (Fig. 7a) characteristically show two dominant Lorentzian features [19] with 6–15 cm^{-1} (FWHM) linewidth at room temperature, the lower frequency component associated with vibrations along the circumferential direction (ω_G^-), and the higher frequency component (ω_G^+) attributed to vibrations along the direction of the nanotube axis. In contrast, the Raman spectra for metallic nanotubes [Fig. 7(b)] also have two dominant components with similar origins, but in this case, the upper frequency component ω_G^+ has a Lorentzian lineshape that is almost as narrow as that for the semiconducting nanotubes, but the lower frequency component ω_G^- is a very broad Breit–Wigner–Fano line (see Fig. 7b), with

a strong coupling to a continuum identified with surface plasmons [25], as discussed further in Section 3.4.

Experimental polarization studies on SWNT bundles [26] show that the G-band for a general chiral nanotube consists of six vibrational modes of $A + E_1 + E_2$ symmetry along each of the two orthogonal (the axial and circumferential) directions [2], consistent with theoretical predictions, as discussed in Section 3.3. Knowledge of the number of modes is important for the lineshape analyses that are used to carry out detailed studies of the G-band properties. Because of the antenna effect (see Section 3.3), the strongest coupling of the $\vec{E}$-field of the laser excitation to the nanotube occurs for the optical $\vec{E}$-field along the nanotube axis, and the most intense modes are found experimentally to be those with A symmetry. It is the curvature of the nanotube which admixes a small amount of interplanar graphene modes into the SWNT circumferential modes, thus lowering their C–C force constants and mode frequencies, as discussed in Section 3.5 and shown in Fig. 7c, where it is seen that ω_G^+ shows no d_t dependence, while ω_G^- has a strong d_t^{-2} dependence, that differs according to whether the nanotubes are semiconducting or metallic. A dependence of the Raman lineshapes and intensity on chiral angle was predicted theoretically [13,27,28], and was also observed experimentally, as is discussed in Section 3.4, but a detailed study at the single nanotube level has not yet been carried out. Studies of the dependence of the Raman G-band lineshape and intensity on d_t, E_{laser}, laser intensity, and $E_{laser} - E_{ii}$ at the single nanotube level also need to be carried out.

Whereas the linewidths for the semiconducting nanotubes do not vary much with diameter, the linewidth for the circumferential mode for metallic nanotubes increases very substantially with decreasing d_t, reflecting the increased Breit–Wigner–Fano coupling, as discussed in Section 3.4. Recent studies have shown that the G-band linewidths are not sensitive to chiral angle θ, or to $E_{laser} - E_{ii}$.

3.3. Polarization and antenna effects

From a theoretical standpoint, zone-folding of the graphene sheet to form a nanotube gives rise to Raman-active modes with $A + E_1 + E_2$ symmetry [2] in both the longitudinal (along the tube axis) and transverse (in the circumferential) directions, in addition to a large number of modes with E_3, E_4, ... symmetry, which are not Raman-active [2]. Experimental polarization studies on nanotube bundles [26], with an average nanotube diameter $d_t \simeq 1.85$ nm and with $E_{laser} = 2.41$ eV, have verified the presence of these six modes (three axial and three circumferential modes). These studies have given explicit values for the polarization parameters, namely for the mode frequencies and relative intensities, for each of these six modes for this particular sample [26]. Curvature of the nanotubes is expected to admix some out-of-plane graphite-derived modes with the circumferential G-band mode, and thereby to weaken the bonds and lower the force constants in the circumferential direction, and, in fact, lower the symmetry of the SWNTs relative to that for the graphene lattice structure. Because of the dependence of the bond directions on chiral angle, a dependence of the polarization parameters on chiral angle θ is expected, and this effect can only be measured at the single nanotube level. Since curvature effects become more prominent as the nanotube diameter d_t decreases, a dependence of the polarization parameters on d_t is also expected. Since the Raman lineshapes and therefore the scattering mechanism for metallic and semiconducting tubes are different from one another, it is expected that the polarization parameters will depend on whether the tubes are semiconducting or metallic. The detailed dependence of the polarization parameters on d_t and E_{laser} has not yet been investigated for SWNT bundles.

Polarization studies at the single nanotube level [29] are attractive from two standpoints. Firstly, the geometrical alignment of the optical $\vec{E}$-field relative to the nanotube axis can be done more directly. Secondly, investigation of the detailed polarization behavior of single nanotubes with known (n, m) can be carried out.

Detailed polarization measurements on individual SWNTs are also expected to be sensitive to the depolarization or antenna effect which refers to the tendency of the nanotubes themselves to create a strong local dipole field, so that the optical electric field seen by the nanotube is the vector sum of the applied field and the local field due to the nanotube antenna. Since the local dipole field is very strong, nanotubes act like polarizers by effectively aligning the applied optical electric field along the nanotube axis. This antenna effect has been shown to be highly effective for metallic nanotubes [30], and the antenna effect has been studied in detail for a single nanotube or a very thin nanotube bundle containing only a few nanotubes, as shown in Fig. 8 [30]. In this work, Duesberg et al. showed that the Raman spectra from a metallic SWNT are strongly suppressed when the light is polarized perpendicular ($\alpha_i = 90°$ in Fig. 8) to the nanotube axis [30].

Polarization measurements at the single nanotube level show that also for isolated semiconducting nanotubes the component polarized normal to the nanotube axis is completely quenched due to the antenna effect [29]. However, two nanotubes whose axes intersect at some angle, each create their own dipole fields, so that the polarization component normal to one of the nanotube axes no longer is completely suppressed. As a consequence of the strong antenna effect in isolated SWNTs, measurements of the dependence of the intensity of a particular feature in the Raman spectrum as a function of diameter and chiral angle should be carried out with the polarization along the most favorable angle with respect to the nanotube axis of the SWNTs whose lengths should exceed

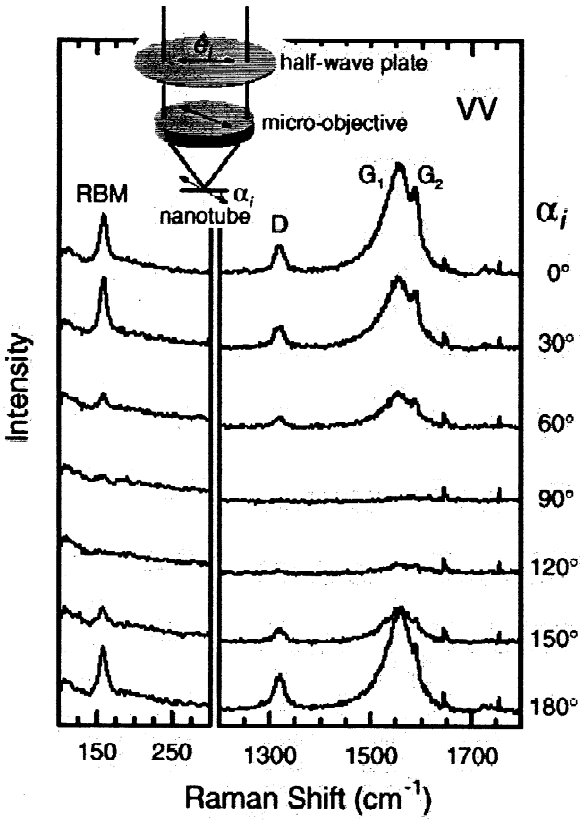

Fig. 8. Raman spectra from a thin SWNT bundle where a metallic nanotube is resonant with $E_{laser} = 1.96$ eV. The spectra were taken with the VV configuration for various angles α_i between the axis of the bundle and the polarization of the incident laser beam, as depicted in the inset. For $\alpha_i = 0°$ and $\alpha_i = 180°$, the polarization of the incident radiation is parallel to the axis of the SWNTs determined from SFM images with an accuracy of $\pm 10°$ [30].

the wavelength of light, and should be longer than the light spot size.

3.4. Lineshapes for metallic and semiconducting nanotubes

The lineshapes of the G-band for semiconducting (S) and metallic (M) nanotubes are qualitatively different. This difference in Raman lineshape is used to readily distinguish between semiconducting and metallic nanotubes, and this lineshape difference is particularly evident at the single nanotube level for tubes with diameters $d_t < 1.7$ nm. Experiments for SWNT bundles show that the upper and lower frequency phonon features are both Lorentzian for semi-conducting tubes, but for the metallic tubes the upper frequency mode is also Lorentzian, while the lower frequency mode has the Breit–Wigner–Fano (BWF) lineshape. Furthermore, the SWNT bundle results show that the frequency of the BWF lower frequency feature for metallic tubes decreases as d_t decreases, while its linewidth increases and its intensity increases [16,25]. Similar effects have been observed for metallic tubes at the single nanotube level, but no detailed studies at the single nanotube level of the BWF parameters ω_{BWF}, Γ_{BWF}, and I_{BWF} have yet been carried out as a function of the variables expected to affect the BWF lineshape, which include θ, d_t, E_{laser}, laser excitation intensity, $E_{laser} - E_{ii}$, and temperature.

Calculations using a bond-polarization model [13] indicate that the lineshape of the G-band for semiconducting nanotubes should be highly sensitive to the nanotube chirality, since the relative intensities of the various G-band components are expected to exhibit a strong dependence on chiral angle as shown in Fig. 9. The dependence on chiral angle of the bond orientations provide the physical reason why the lineshape for the G-band should show a strong dependence on chiral angle. Such chirality-dependent effects cannot be easily studied on SWNT bundles and require measurements at the single nanotube level. Evidence for a chirality dependence of the relative intensities of the axial and circumferential components of the G-band in semiconducting tubes from the work of Yu and Brus [24] is shown in Fig. 10, where spectra are presented for six different thin bundles (containing only a very few tubes), with presumably only one of the tubes resonant at the two different laser excitation energies that were used in this work. In Fig. 10a only the higher frequency axial vibrational feature is seen, Fig. 10f shows equal intensities for the higher and lower frequency

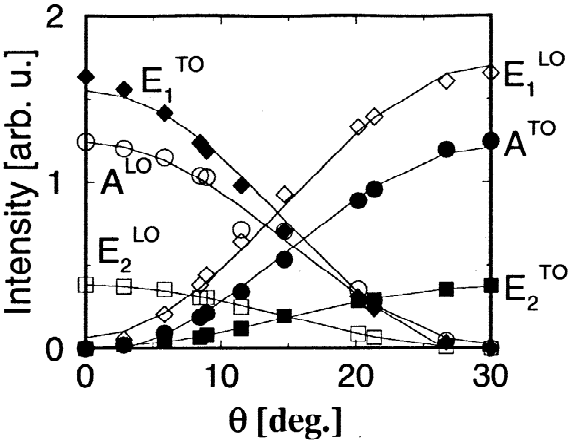

Fig. 9. The calculated chirality dependence for the intensities of the G-band LO and TO modes for single wall carbon nanotubes, based on a bond-polarization model [13]. In this figure LO and TO, respectively, refer to vibrations along the nanotube axis and in the circumferential direction.

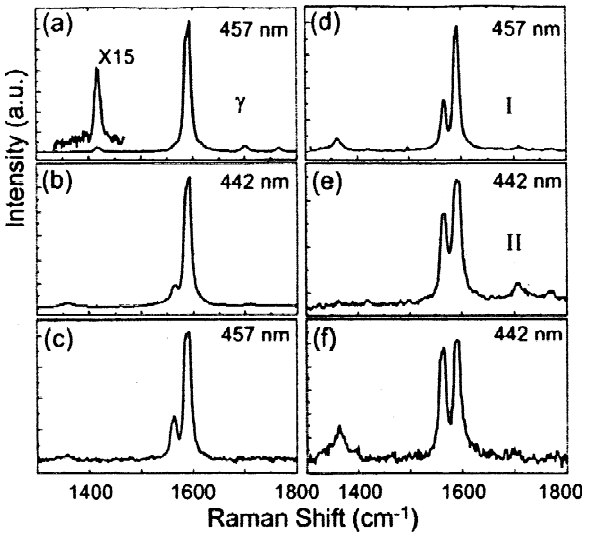

Fig. 10. Raman spectra of semiconducting SWNTs in six different thin bundles (a–f) in the range 1300–1800 cm^{-1}. The excitation wavelength is 457 nm (2.71 eV) for the spectra in (a), (c), and (d) and 442 nm (2.80 eV) for the spectra in (b), (e), and (f). A laser excitation intensity of 40 kW/cm^2 was used for these experiments. The inset to part (a) shows a magnified view of the 1417-cm^{-1} D-band Raman peak [24].

features, and the other traces show various intermediate intensity ratios, with Fig. 10c showing a spectrum most similar to that obtained from typical SWNT bundles containing many SWNTs.

3.5. Diameter dependence of ω_G

Calculations using the bond-polarization model, considering atomic interactions up to fourth nearest neighbors show that the eigenvectors for the G-band modes have vibrations either along the nanotube axis or perpendicular to it, with G independent of chiral angle for nanotubes of approximately the same diameter [13,27], thereby justifying the analysis of the experimental data for ω_G in terms of ω_G^+ and ω_G^- as is done in Fig. 7. Considering that long distance force constants contribute to the normal mode vibrations, the nanotube system looks like a homogeneous cylinder, and the curvature effect is predicted to result in a splitting of the G-band modes.

As has already been pointed out, the two most important features in the G-band profile for SWNTs are associated with phonons of A symmetry. The experimental spectra in Fig. 7a for semiconducting SWNTs show a clear difference in the $(\omega_G^+ - \omega_G^-)$ splitting between the axial and circumferential modes from one semiconducting nanotube to another. Inspection of Fig. 7b shows that the $(\omega_G^+ - \omega_G^-)$ splitting appears to be qualitatively different in magnitude for metallic and semiconducting nanotubes. In Fig. 7c it is seen that ω_G^+ is independent of d_t and is the same for semiconducting and metallic SWNTs, while ω_G^- is strongly dependent on d_t and is well fit to the functional form

$$\omega_G^- = \omega_G^+ - \mathscr{C}/d_t^2 \tag{4}$$

where $\mathscr{C} = 47.7$ cm^{-1} nm^2 for semiconducting nanotubes and $\mathscr{C} = 79.5$ cm^{-1} nm^2 for metallic nanotubes. At the single nanotube level, no chirality dependence for the G-band ω_G^+ and ω_G^- mode frequencies is found experimentally, nor is $\mathscr{C}$ found to depend on E_{laser}. Therefore it is convenient to use Eq. (4) to obtain an approximate determination of d_t for those SWNTs where the RBM feature is not observed. Polarization studies tell us that for measurements carried out on randomly aligned nanotubes in SWNT bundle samples, the spectra are dominated by modes of *A* symmetry, and the antenna effect, that is responsible for a strong enhancement of the axial *A* symmetry mode relative to the other modes, is most pronounced at the single nanotube level.

Analysis of the G-band spectra at the single nanotube level shows that the effect of curvature on the $(\omega_G^+ - \omega_G^-)$ splitting is generally larger than that introduced by the zone folding effect [31] for the nanotube diameter range that is commonly studied. At present, there is no detailed theoretical model for the magnitudes of $\mathscr{C}$, nor is there an explanation for the different $\mathscr{C}$ values for semiconducting and metallic nanotubes, though the $1/d_t^2$ dependence is compatible with the weakening of the C–C force constants through admixture of weak interplanar graphite modes through the nanotube curvature effect.

4. D-band and G′-band

4.1. Overview

The D-band and G′-band features are both observed in the Raman spectra of semiconducting and metallic SWNTs at the single nanotube level as seen in Fig. 1a. The frequency of the disorder-induced D-band ($1250 < \omega_D < 1450$ cm^{-1}) and of its second-order overtone G′-band ($2500 < \omega_{G'} < 2900$ cm^{-1}) in the Raman spectra of sp^2-bonded carbon materials has been known for many years to exhibit a strongly dispersive behavior as a function of laser excitation energy ($1.0 < E_{laser} < 4.5$ eV) [32,33]. The strong linear dispersion $\omega_D(E_{laser})$ of the D-band frequency $\omega_D(E_{laser})$ in graphite (53 cm^{-1}/eV), and of its second-order overtone G′-band (10^6 cm^{-1}/eV), has been identified with a resonance process between a phonon and an electronic transition between linearly dispersive π and π* states [34–37]. The double resonance model shown in Fig.

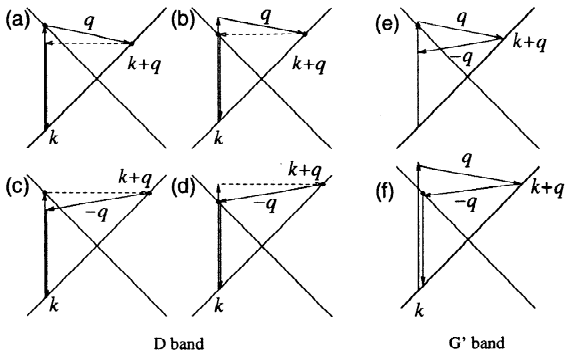

Fig. 11. (a–d) Four different D-band double resonance Stokes processes in graphite which all involve second-order, one-phonon emission processes. For each process, the dashed lines denote the elastic scattering process and small black dots denote the resonant points. (e,f) The corresponding G′-band processes which involve second-order, two-phonon emission processes. The dashed lines of each figure for the D-band process become an inelastic phonon emission process, and thus only the (a) and (d) processes, shown as (e) and (f) with appropriate modification, are possible in two-phonon processes [38].

11 in particular [34,36,38] accounts for the observed dispersion of the D-band and the G′-band as a function of photon excitation energy E_{laser} in graphite and in sp^2 carbons. In Section 4.2 a single extension of this model to account for the special properties of the D-band and G′-band of isolated SWNTs is presented.

The Raman spectra taken on SWNT bundles indicate that the D-band and G′-band features have dispersion relations that are generally similar to those in other sp^2 carbons, but also show some distinct characteristic behaviors that are special to nanotubes. A very interesting aspect of the Raman spectra for SWNT bundles is the observation of a step or oscillatory effect in the D-band dispersion relation (see Fig. 12a,b) [39], an effect not present in other sp^2 carbons. One objective of Raman spectroscopy studies at the single nanotube level is to gain an understanding of this effect, and this topic is discussed in Section 4.3, in connection with the dependence of the D-band and G′-band features on the SWNT electronic structure. In Section 4.4, diameter and chirality-dependent D-band and G′-band effects, observed at the single nanotube level, are discussed, with particular reference to

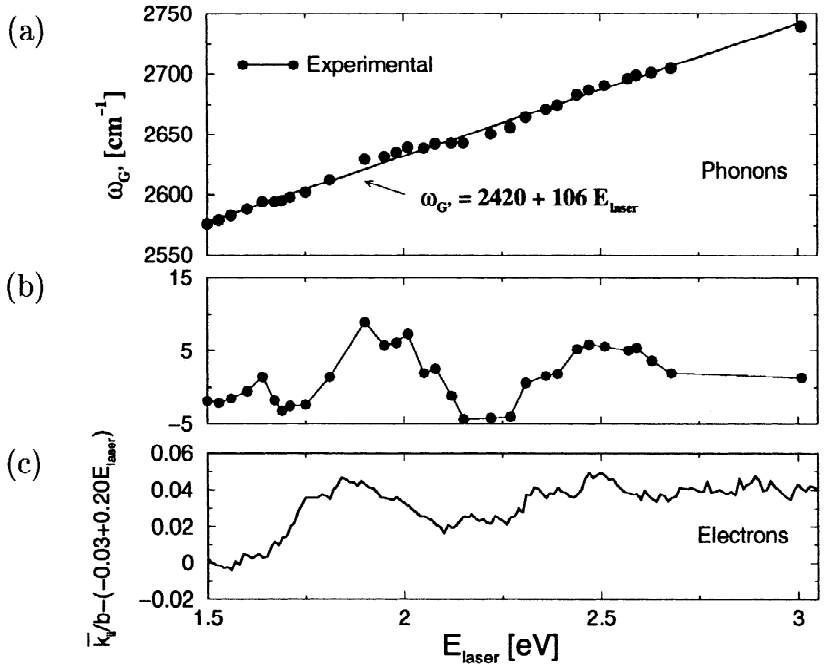

Fig. 12. (a) Dependence on the laser excitation energy of $\omega_{G'}$ for the dominant second-order Raman feature for single wall carbon nanotube (SWNT) bundles. In contrast to most sp^2 carbons where $\omega_{G'}$ depends linearly on E_{laser}, the corresponding plot for SWNT bundles shows a superimposed step-like or oscillatory behavior near 2.0 and 2.5 eV for SWNT bundles. (b) The oscillatory component of (a) obtained after subtracting the linear background given by $\omega_{G'} = 2420 + 106E_{laser}$ in (a). (c) Plot of the E_{laser} dependence of the oscillations in the resonant electron wave vector k_{ii} after normalization to the length of the basis vector b of the reciprocal lattice of 2D graphite and after subtracting the linear background. For each E_{laser} value, the k_{ii} values for each resonant SWNT are calculated, and $\bar{k}_{ii}$ represents an appropriate weighted average [41]. The strong correspondence between the E_{laser} dependence of $\omega_{G'}$ for phonons and $\bar{k}_{ii}$ for electrons provides strong support for the identification of each oscillation with a particular interband transition between van Hove singularities [41].

explaining the anomalous behavior of the D-band and G′-band dispersion relations for carbon nanotube bundles. New physical phenomena related to the resonance Raman process itself can be seen in the G′-band spectra of individual nanotubes under special circumstances, involving a double resonance process with both the E_{33}^{S} and E_{44}^{S} interband transitions [18], and this is discussed in Section 4.5 in connection with the strong resonant enhancement that occurs through the 1D JDOS, utilizing the strong dispersion of the G′-band as a function of E_{laser}. This two peak G′-band effect can be used to confirm independently the (n, m) structural characterization carried out through analysis of the radial breathing mode feature, as discussed in Section 2.2. The G′-band feature is attractive for a variety of fundamental investigations of the special properties of the electronic structure of SWNTs, utilizing their very large dispersion (106 cm^{-1}/eV in SWNT bundles [39]), allowing frequency shifts to be observed in $\omega_{G'}$ through the resonance Raman effect which can directly probe the detailed properties of the electronic structure.

4.2. Mechanism responsible for the D-band and G′-band

In contrast to the RBM and G-band features in the Raman spectra for SWNTs which relate to the zone center of the Brillouin zone and are non-dispersive (i.e., the Raman shift is independent of laser excitation energy), both the D-band and G′-band features relate to the region near the K-point of the 2D graphite Brillouin zone and are highly dispersive, showing a strong dependence of ω_D and $\omega_{G'}$ on the laser excitation energy for SWNT bundles. The physical origin of the D-band and G′-band features in the Raman spectra in isolated SWNTs is based on the double resonance mechanism which is operative for graphite [36,40], but is modified in SWNTs by the 1D van Hove singularities that dominate the electron density of states. The double resonance effect in graphite occurs when both the initial (or final) state and the scattered intermediate state are actual electronic states.

In the Stokes (phonon emission) D-band process for graphite, an electron with momentum k and energy $E_i(k)$ is excited by the incident laser photon in an electron–hole pair creation process. The electron is then scattered by emitting a phonon with momentum q to the state with momentum $k+q$ and energy $E(k+q)$, as indicated in Fig. 11a,b. The electron is then scattered back to k [$E_f(k)$] to recombine with a hole. In the one-phonon emission process shown in Fig. 11a–d, one of the two scattering processes ($k \rightarrow k+q$, or $k+q \rightarrow k$) is inelastic with the emission of a phonon, and the other is an elastic scattering process associated with a defect (dashed lines in Fig. 11). Thus we can expect four different double resonance Raman processes for the D-band, as shown in Fig. 11a–d schematically, to make important contributions to the Raman intensity for a Stokes form. These four resonant conditions for the D-band in graphite can be expressed by:

$$
\begin{aligned}
&(a)\quad \mathbf{E_i}(\mathbf{k}) = E_L,\\
&\qquad \mathbf{E}(\mathbf{k}+\mathbf{q}) = \mathbf{E_i}(\mathbf{k}) - \hbar\omega_{ph}(q),\\
&\qquad E_f(k) = \mathbf{E}(\mathbf{k}+\mathbf{q}),\\
&(b)\quad E_i(k) = E_L,\\
&\qquad \mathbf{E}(\mathbf{k}+\mathbf{q}) = E_i(k) - \hbar\omega_{ph}(q),\\
&\qquad \mathbf{E_f}(\mathbf{k}) = \mathbf{E}(\mathbf{k}+\mathbf{q}),\\
&(c)\quad \mathbf{E_i}(\mathbf{k}) = E_L,\\
&\qquad \mathbf{E}(\mathbf{k}+\mathbf{q}) = \mathbf{E_i}(\mathbf{k}),\\
&\qquad E_f(k) = \mathbf{E}(\mathbf{k}+\mathbf{q}) - \hbar\omega_{ph}(-q), \text{ and}\\
&(d)\quad E_i(k) = E_L,\\
&\qquad \mathbf{E}(\mathbf{k}+\mathbf{q}) = E_i(k),\\
&\qquad \mathbf{E_f}(\mathbf{k}) = \mathbf{E}(\mathbf{k}+\mathbf{q}) - \hbar\omega_{ph}(-q),
\end{aligned}
\tag{5}
$$

in which the bold face denotes the existence of an actual electronic state which satisfies the resonant condition. The anti-Stokes process (phonon absorption) is related by time-reversal symmetry to the Stokes processes, shown in Fig. 11. For the G′-band ($\omega_{G'} \simeq 2\omega_D$) which is a two-phonon process, the elastic scattering process denoted by a dashed line in Fig. 11a–d is replaced by an inelastic phonon emission process. Therefore, only cases (a) and (d), and shown in Fig. 11e,f, are possible for the double resonance processes for the G′-band. The phonon q vector for both the D-band and the G′-band resonance processes is related to the resonant electron k vector by the relation $|q| \simeq 2|k|$ where k is measured from the K-point in the Brillouin zone [38].

Since the D-band in graphite involves scattering from a defect which breaks the basic symmetry of the graphene sheet, it is observed in sp^2 carbons containing vacancies, impurities, or other symmetry-breaking defects. On the other hand, the second-order G′-band does not require an elastic defect-related scattering process, and is observable for defect-free sp^2 carbons. The special properties of the electronic structure of SWNTs enter the double resonance process through van Hove singularities occurring in the electronic states $E_i(k)$, $E_f(k)$, and $E(k+q)$, which give rise to singularities in the joint density of states at the E_{ii} interband transitions. In this way it is possible to gain sufficient Raman intensity to produce strong D-band and G′-band features in the Raman spectra from one isolated semiconducting or metallic nanotube. Experimentally, semiconducting and metallic nanotubes which are in resonance with the incident photon generally exhibit D-band and G′-band features at the single nanotube level, in addition to the RBM and G-band features.

4.3. General D-band and G′-band properties

One of the unique features of the D-band and the

G′-band spectra of SWNT bundles is a step or oscillatory behavior [39,42,43] superimposed on the linear E_{laser} dependence of both ω_D and $\omega_{G'}$ that is characteristic of graphite and sp^2 carbons. This effect is shown for the G′-band in Fig. 12a, but also appears in the corresponding plot of ω_D versus E_{laser}. The deviation from a linear dispersive behavior is clearly seen in Fig. 12b, where the points are obtained after subtraction of the linear solid line fit to the experimental points in Fig. 12a. The oscillatory behavior in Fig. 12b is identified with quantum effects associated with the strong coupling between the electrons and phonons under resonance conditions. Specifically the peak near 2.0 eV is identified with the E_{11}^{M} interband transition for metallic nanotubes and the peak near 2.5 eV with the E_{33}^{S} and E_{44}^{S} transitions for semiconducting nanotubes, thus showing the importance of the 1D electronic structure of SWNTs in the physical origin of the D-band and the G′-band spectra. The physical basis for this step or oscillatory behavior was explained by the coupling between electrons and phonons under resonance conditions, which depends on both the diameter and chirality of the resonant nanotubes, as elucidated at the single nanotube level.

The dependence of ω_D and ω'_G on d_t and θ, are presented in Section 4.4. While ω_D and $\omega_{G'}$ have unique values for a given E_{laser} in sp^2 carbons, the behavior for SWNTs is quite different, and a given value of E_{laser} can result in a range of ω_D and $\omega_{G'}$ values depending on the nanotube diameter d_t (Fig. 13) and chiral angle θ (Fig. 14), as is discussed in Section 4.4. Both ω_D and $\omega_{G'}$ are, in fact, found to decrease as d_t decreases, as would be expected both from the effect of nanotube curvature on the softening of these mode frequencies and from the electron–phonon interaction discussed in Section 4.4. Furthermore, the values of ω_D and $\omega_{G'}$ are found to be larger for metallic SWNTs than for semiconducting SWNTs of the same diameter [17], suggestive of a somewhat different scattering mechanism for semiconducting and metallic nanotubes, but a detailed understanding of these differences requires additional research. No systematic experimental or theoretical study of the D-band and G′-band linewidths has yet been carried out.

A random D-band intensity variation is observed from one nanotube to another, consistent with the identification of the D-band in carbon nanotubes with defects. To date there has been no systematic study of the various dependences that influence the D-band and the G′-band intensities.

The laser excitation energy E_{laser} is expected to influence many aspects of the D-band and the G′-band Raman features, but the E_{laser} dependence of ω_D and $\omega_{G'}$ has so far only been studied systematically for SWNT bundles. In view of the interesting quantum mechanical effects that are observed in the E_{laser} dependence of $\omega_D(E_{laser})$ and $\omega_{G'}(E_{laser})$, systematic study of other Raman parameters, such as the linewidth and intensity as a function of E_{laser}, would also be expected to yield interesting experimental and theoretical results.

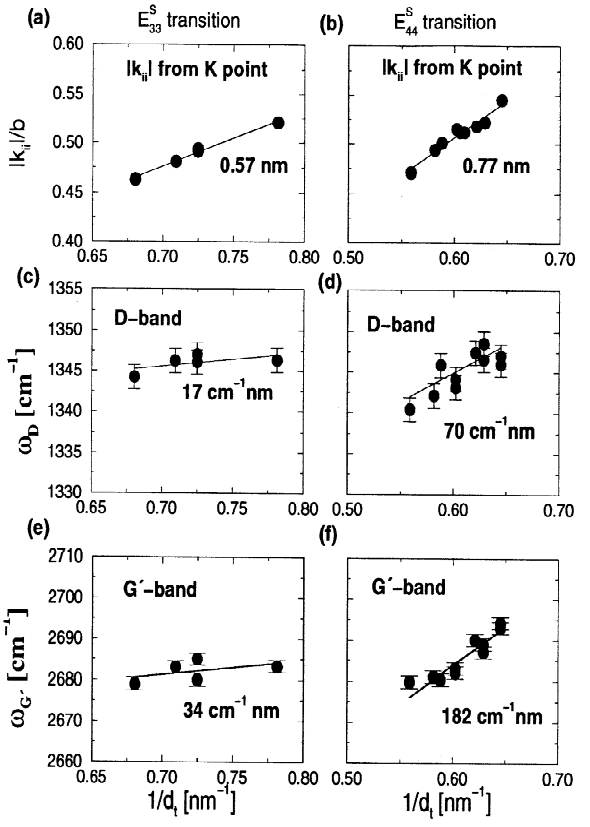

Fig. 13. The calculated values of $|k_{ii}|$ as measured from the K-point in the Brillouin zone for interband transitions E_{33}^{S} (a) and E_{44}^{S} (b) for electronic states in isolated SWNTs in resonance with $E_{laser}=2.41$ eV. The $|k_{ii}|$ values are normalized to the reciprocal lattice vector length b for graphite, and numerical values for the slopes $\partial(|k_{ii}|)/b|/\partial(1/d_t)$ are given for the two upper figures (a) and (b). D-band frequencies for isolated SWNTs, as a function of reciprocal diameter $1/d_t$, that are in resonance with the (c) E_{33}^{S} and (d) E_{44}^{S} interband transitions. (e) and (f) plot the same variables as in (c) and (d), respectively, except that the data are for the G′-band. Values for the slopes of $\partial\omega_D/\partial(1/d_t)$ and $\partial\omega_{G'}/\partial(1/d_t)$ are given for the four lower figures.

4.4. Nanotube diameter and chirality-dependent effects

The (n, m) dependences of the mode frequencies, ω_D and $\omega_{G'}$ are interesting in their own right, because of their curious dependence on chiral angle θ and nanotube diameter, which relates to the electronic mechanism giving rise to the D-band and the G′-band features in the Raman spectra. What we mean by diameter and chiral angle dependence for SWNTs is that different nanotubes with different d_t and θ values will be resonant at the same E_{laser}

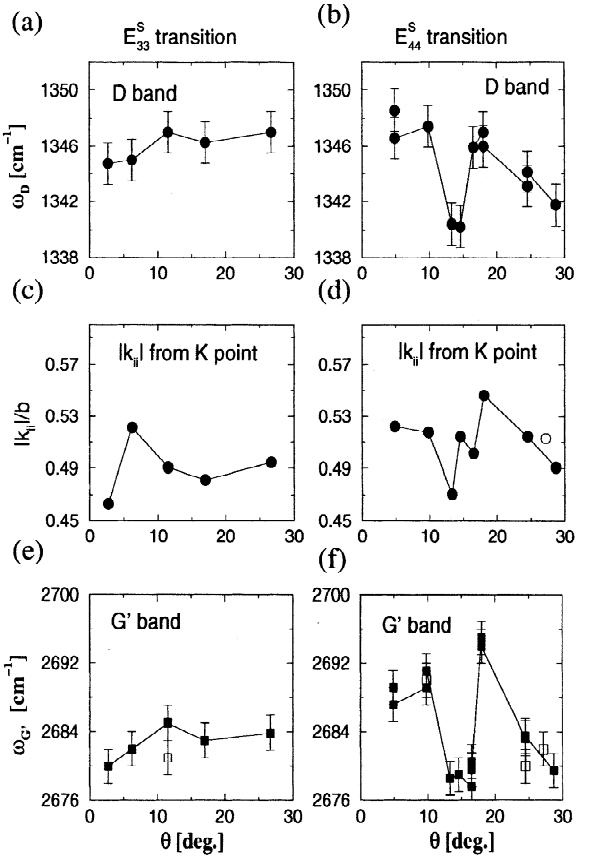

Fig. 14. D-band frequencies $\omega_D(\theta)$ as a function of chiral angle θ of the tubes for which the laser energy ($E_{laser}=2.41$ eV) is resonant with the E^S_{33} (a) and E^S_{44} (b) interband transitions in the JDOS. The distance $|k_{ii}|$ from the K-point in the 2D graphene Brillouin zone for the electronic states corresponding to the van Hove singularities in the JDOS E^S_{33} (c) and E^S_{44} (d), respectively, for the various nanotubes measured in (a) and (b). In (c) and (d), $|k_{ii}|$ is normalized to b, the length of the reciprocal lattice basis vector of the 2D graphite lattice. Figures (e) and (f) are the same as in (a) and (b), respectively, except that the data are for the G′-band. The solid (open) squares in (e) and (f) denote $\omega_{G'}(\theta)$ data for tubes where the D-band is (not) observed in the Raman spectrum [41].

value, thus giving rise to a range of ω_D and $\omega_{G'}$ values, whereas for sp^2 carbons and graphite there is a single ω_D and a single ω'_G value for a given E_{laser}. In Fig. 14 we show that ω_D and $\omega_{G'}$ both have a dependence on chiral angle θ for nanotubes with a similar diameter, whereas ω_{RBM} and ω_G do not show any significant dependence on θ. Furthermore, Fig. 14 shows that the detailed dependence of ω_D and ω_G on chiral angle depends on which interband transition E_{ii} is involved in the resonance Raman process. To identify the origin of the θ dependence of ω_D and $\omega_{G'}$, we plot $\omega_D(\theta)$ in Fig. 14(a) for the E^S_{33} transitions and in Fig. 14(b)d for the E^S_{44} transitions. The corresponding θ dependence of $|k_{ii}|/b$ is shown in Fig. 14(c) and (d), where k_{ii} is the electron wavevector measured from the K-point corresponding to the singularity E_{ii} in the joint density of states and b is the length of the basis vector in the reciprocal lattice of 2D graphite. The similarity between the θ dependence of ω_D and $|k_{ii}|/b$ is consistent with the connection between the resonant electronic state k_{ii} and the wavevector of the phonon that is emitted in the D-band process. The similarity of the θ dependence of ω_D and of $\omega_{G'}$ suggests that the mechanisms responsible for the D-band and G′-band scattering are related. Finally, the fact that the θ dependence of $\omega_{G'}$ for those nanotubes that show no D-band feature and is consistent with $\omega_{G'}$ for nanotubes that do show D-band scattering intensity indicates that the mechanism responsible for the G′-band in SWNTs does not depend on the presence of defects, as is also the case for other sp^2 carbons.

The nanotube diameter dependence of ω_D is shown in Fig. 13, for $E_{laser}=2.41$ eV, where each point corresponds to a different SWNT in resonance with E_{laser}. Here it is seen that the d_t dependence is different for each subband E^S_{33} and E^S_{44} (Fig. 13c and d, respectively), but for each individual subband, ω_D shows a linear dependence on $1/d_t$ according to $\omega_D=\omega_D^{0,i}-\beta_i/d_t$ with slopes β_i that differ according to which E_{ii} is in resonance with E_{laser}. The fact that $\omega_{G'}\sim 2\omega_D(d_t)$ and $\omega_{G'}(d_t)$ show the same dependence on E_{ii} indicates that a similar physical mechanism is responsible for the D-band and the G′-band features in the Raman spectra for individual SWNTs (see Fig. 13e,f). When plotted over a large range of d_t, a simple picture for the d_t dependence of ω_D and $\omega_{G'}$ emerges, which in turn clarifies the relation between $\omega_D(d_t)$ for SWNT bundles and isolated SWNTs. The diameter dependence of SWNT bundles and of isolated SWNTs both show a $1/d_t$ dependence and an extrapolation of ω_D to ω_D^0 for a graphene sheet in the limit $d_t\to\infty$. The value of $\beta=16.9$ cm^{-1} nm provides a good fit to $\omega_D=\omega_D^0-\beta/d_t$ for typical SWNT bundles. Preliminary measurements indicate that β for metallic nanotubes (i.e., for the E^M_{11} interband transitions) is greater than for the semiconducting nanotubes (i.e., for E^S_{33} and E^S_{44} transitions) [17], but this needs further quantitative study. Because of the $E_{ii}\propto 1/d_t$ dependence, resonances within a given E_{ii} transition occur at higher E_{laser} values as the tube diameter decreases. For this reason the dispersion relations $\omega_D(E_{laser})$ and $\omega_{G'}(E_{laser})$ are sensitive to nanotube diameter. Once the lower diameter limit of the sample is reached, resonances are made with the next higher lying E_{ii}, starting with the largest d_t nanotube in the SWNT bundle. The ω versus E_{laser} curves thus show step-like decreases, as each new interband transition comes into play (see Fig. 12b). This diameter-dependent ω_D and $\omega_{G'}$ behavior competes with the linear ω_D and $\omega_{G'}$ versus E_{laser} dependence, that relates to the double resonance phenomena associated with the K-point of the Brillouin zone of sp^2 carbons, to give rise to a step-like or oscillatory behavior, superimposed on the

linear dispersion relation that is observed for almost all sp^2 carbon materials [17]. The observations of the oscillatory behavior in ω_D and $\omega_{G'}$ versus E_{laser} in Fig. 12a,b were made for resonance with E_{11}^M for metallic nanotubes within SWNT bundles, and with E_{33}^S and E_{44}^S for semiconducting nanotubes within these same bundles [17]. By considering this diameter and chirality-dependent behavior at the single nanotube level, the features observed experimentally can be explained quantitatively [41], and the mechanism responsible for this oscillatory behavior can be identified with a resonance Raman process that is highly sensitive to the van Hove singularities in the electronic density of states.

The identification of nanotube properties that show a characteristic chirality dependence is interesting at present, because of the need to find ways for self assembling nanotubes of the same chiralities in the growth process. The θ dependence of ω_D and $\omega_{G'}$ might find some interesting applications in this connection.

4.5. Two-peak structure in the G′-band

In the observation of the G′-band Raman spectra from isolated individual nanotubes, most of the spectra are single Lorentzian lines. However, in some cases a two-peak structure has been observed for isolated SWNTs whose (*n*, *m*) indices have been identified from analysis of their radial breathing modes [18]. Fig. 15a shows such a two-peak structure in the experimental G′-band profile for a (15,7) nanotube excited by $E_{laser}=2.41$ eV. From the (*n*, *m*) indices determined from the radial breathing mode analysis, the E_{44}^S and E_{33}^S interband transitions can be calculated, and the results are shown on the right, where it is seen that the E_{44}^S transition is within the resonant window for the incident photon $E_{laser}=2.41$ eV), while the E_{33}^S transition is within the resonant window for the scattered photon ($E_{laser}-E_{G'}\simeq 2.41-0.33=2.08$ eV). The two-peak structure in the G′-band can be observed when the double resonance process in Fig. 11e occurs for the incident photon with the E_{44}^S transition, and in Fig. 11f occurs for the scattered photon with the E_{33}^S transition. The strong G′-band dispersion $\omega_{G'}(E_{laser})$ in SWNTs allows sufficient resolution of the splitting in the phonon frequency $\omega_{G'}$ to observe the two peaks associated with each of the (e) and (f) double Raman resonance processes in Fig. 11. Verification of the proper identification of this physical process comes from the excellent agreement

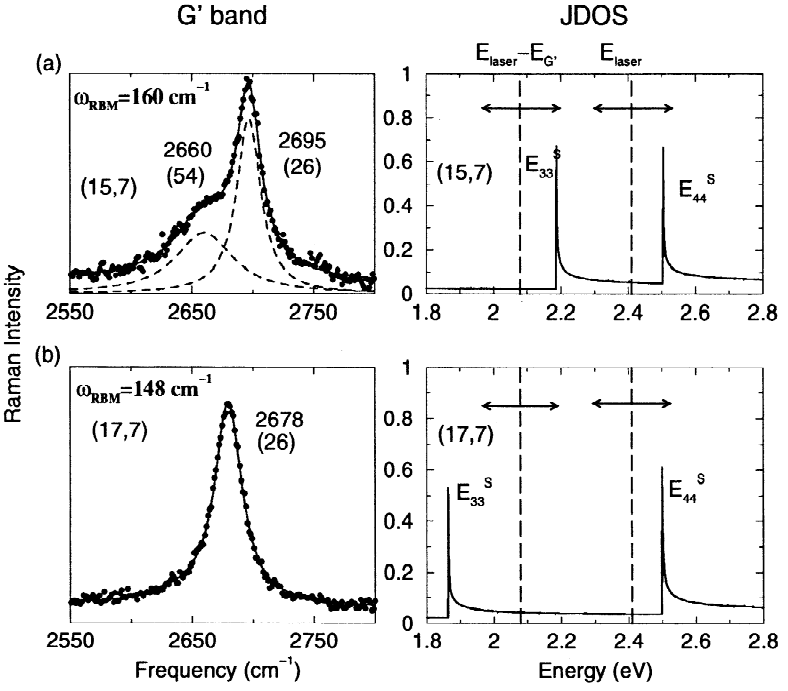

Fig. 15. G′-band phonon profile (left panels) and joint density of electronic states (right panels) for (15, 7) and (17, 7) SWNTs. The G′-band profile for the (15, 7) tube has two peaks, indicating that the resonance is occurring with both the incident and scattered photons, as depicted in the joint density of states display (right panel). The incident photon with energy E_{laser} is resonant with E_{44}^S for both the (15, 7) and (17, 7) SWNTs. The scattered photon is resonant with E_{33}^S for the (15, 7) tube, but not for the (17, 7) tube. The vertical dashed lines represent $E_{laser}=2.41$ eV and $E_{laser}-E_{G'}\approx 2.08$ eV for the incident and scattered photons, respectively. The horizontal double arrows denote the resonant windows for the incident and scattered photons. The numbers in parentheses denote the linewidths, and all frequencies and linewidths are in units of cm^{-1} [18].

between theory and experiment regarding the special (n, m) values where the two-peak spectrum is expected, and the other (n, m) values where the G′-band resonance occurs with only a single transition, as is the usual case for the G′-band profile. The two-peak G′-band resonance process is explicitly illustrated in Fig. 15a for a (15, 7) nanotube, where the incident photon is in resonance with E^{S}_{44} and the scattered photon is in resonance with E^{S}_{33}. In contrast, we show in Fig. 15(b) the spectrum for a (17, 7) nanotube, where the incident photon is clearly in resonance with E^{S}_{44}, while E^{S}_{33} is clearly outside of the resonance window for the scattered photon. Having made a correct identification for those (n, m) nanotubes which should exhibit this two-peak Raman effect and those nanotubes which should not, for a collection of 16 different nanotubes, we can then turn around and use the presence or absence of the two-peak phenomenon of the G′-band with the E^{S}_{33} and E^{S}_{44} transitions as an internal check on the (n, m) assignment of a given nanotube from its RBM spectrum (see Section 2.2). Such internal consistency checks are important for establishing confidence in the utilization of single nanotube spectroscopy as a reliable method for SWNT structural characterization and for studying new quantum-based phenomena in carbon nanostructures.

5. Summary

In this review, we have emphasized the role that the van Hove singularities in the 1D density of electronic states play in making possible the observation of Raman spectra of the phonon modes from one isolated carbon nanotube, through the strong electron–phonon coupling that occurs under resonance conditions when an incident or scattered photon matches the energy of an electronic transition in a single wall carbon nanotube [44]. The very narrow width of the van Hove singularity in the joint density of states, measured by the resonance Raman effect using a tunable laser, shows directly why single nanotube Raman spectroscopy is possible.

Though Raman scattering is not generally a structural characterization tool, the unique 1D molecular nature of SWNTs makes the resonance Raman technique an extremely useful and accurate method for the identification of the (n, m) indices or alternatively of the diameter and the chirality of an individual SWNT. The Raman technique is especially attractive for such structural characterization because it is a weakly interactive probe, nondestructive, readily available, and the measurements are made at room temperature without heating the SWNT.

The value for the tight binding nearest neighbor overlap energy γ_0 used for the electronic structure calculations in this work may be different from the values of γ_0 that have been used in the interpretation of the STM experiments. The reasons for this difference in γ_0 are not presently understood but may be related to the gold substrate used in STM experiments and to the different approximations made in the tight binding calculations for the scanning tunneling spectra and for the resonance Raman process. Further work is needed to clarify this point.

The single nanotube spectra provide valuable information about every feature of the Raman spectra for individual nanotubes, including both the non-dispersive Raman-allowed radial breathing mode and the tangential G-band mode also present in graphite, as well as the D-band and its second-order G′-band which are highly dispersive in graphite. The information provided by the disorder-induced D-band and by the symmetry-allowed G′-band is expected to be particularly informative about the resonance processes giving rise to these features in the Raman spectra for nanotubes. Of particular interest are the many D-band and G′-band phenomena that are shown to be dependent on nanotube diameter and chirality.

Another aspect of single nanotube Raman spectroscopy is its use as a probe of many aspects of the electronic structure associated with the 1D singularities in the joint density of states. In this connection several new effects about the electronic structure or about the resonance Raman effect have been observed for the first time. The use of single nanotube spectroscopy for the (n, m) characterization of individual nanotubes enables one to consider other experiments, such as transport, optical properties, mechanical properties, and thermal properties to be carried out at the single nanotube level to study their dependence on nanotube diameter and chirality in a systematic way.

Acknowledgements

The authors gratefully acknowledge the helpful and informative discussions with Drs. A.K. Swan, J.-C. Charlier, A.M. Rao, H. Kataura, K. Kneipp, M.A. Pimenta, P.C. Eklund, and S.D.M. Brown and the fruitful collaboration with Professors J.H. Hafner and C.M. Lieber who provided the samples needed to carry out the single nanotube Raman experiments. The authors are also thankful to many other colleagues for their assistance with the preparation of this article. The research of the MIT group is supported by NSF grant DMR 01-16042. A.G.S.F. and A.J. acknowledge financial support from CAPES and CNPq-Brazil, respectively, and R.S. acknowledges a Grant-in-Aid (No. 13440091) from the Ministry of Education, Japan.

References

[1] Dresselhaus MS, Dresselhaus G, Eklund PC. In: Science of Fullerenes and Carbon Nanotubes, New York, NY, San Diego, CA: Academic Press, 1996.
[2] Saito R, Dresselhaus G, Dresselhaus MS. In: Physical Properties of Carbon Nanotubes, London: Imperial College Press, 1998.

[3] Dresselhaus MS, Eklund PC. Adv Phys 2000;49:705–814.
[4] Jorio A, Saito R, Hafner JH, Lieber CM, Hunter M, McClure T, Dresselhaus G, Dresselhaus MS. Phys Rev Lett 2001;86:1118–21.
[5] Temple PA, Hathaway CE. Phys Rev B 1973;7:3685–97.
[6] Hafner JH, Cheung CL, Oosterkamp TH, Lieber CM. J Phys Chem B 2001;105:743.
[7] Berber S, Kwon Y-K, Tománek D. Phys Rev Lett 2000;84:4613.
[8] Dresselhaus MS, Dresselhaus G, Avouris P. In: Carbon Nanotubes: Synthesis, Structure, Properties and Applications, Springer Series in Topics in Applied Physics, vol. 80, Berlin: Springer, 2001.
[9] Kataura H, Kumazawa Y, Maniwa Y, Umezu I, Suzuki S, Ohtsuka Y, Achiba Y. Synthetic Metals 1999;103:2555–8.
[10] Dresselhaus G, Pimenta MA, Saito R, Charlier J-C, Brown SDM, Corio P, Marucci A, Dresselhaus MS. In: Tománek D, Enbody RJ, editors, Science and Applications of Nanotubes, Proceedings of the International Workshop on the Science and Applications of Nanotubes, Michigan State University, East Lansing, MI, USA, July 24-27, 1999, New York: Kluwer Academic, 2000, pp. 275–95.
[11] Saito R, Dresselhaus G, Dresselhaus MS. Phys Rev B 2000;61:2981–90.
[12] Odom TW, Huang JL, Kim P, Lieber CM. Nature (London) 1998;391:62–4.
[13] Saito R, Jorio A, Hafner JH, Lieber CM, Hunter M, McClure T, Dresselhaus G, Dresselhaus MS. Phys Rev B 2001;64:5312–9.
[14] Odom T, Hafner JH, Lieber C. In: Dresselhaus MS, Dresselhaus G, Avouris P, editors, Carbon Nanotubes: Synthesis, Structure, Properties and Applications, Springer Series in Topics in Applied Physics, Berlin: Springer, 2001, pp. 173–212.
[15] Saito R, Kataura H. In: Dresselhaus MS, Dresselhaus G, Avouris P, editors, Carbon Nanotubes: Synthesis, Structure, Properties and Applications, Springer Series in Topics in Applied Physics, Berlin: Springer, 2001, pp. 213–46.
[16] Jorio A, Souza Filho AG, Dresselhaus G, Dresselhaus MS, Swan AK, Goldberg B, Ünlü MS, Pimenta MA, Hafner JH, Lieber CM, Saito R. Phys Rev B (2001) BF8180, submitted.
[17] Pimenta MA, Jorio A, Brown SDM, Souza Filho AG, Dresselhaus G, Hafner JH, Lieber CM, Saito R, Dresselhaus MS. Phys Rev B 2001;64:1401.
[18] Souza Filho AG, Jorio A, Dresselhaus G, Dresselhaus MS, Swan AK, Ünlü MS, Goldberg BB, Saito R, Hafner JH, Lieber CM, Pimenta MA. Phys Rev B (2002) submitted.
[19] Jishi RA, Venkataraman L, Dresselhaus MS, Dresselhaus G. Chem Phys Lett 1993;209:77–82.
[20] Kürti J, Kresse G, Kuzmany H. Phys Rev B 1998;58:R8869.
[21] Sanchez-Portal D, Artacho E, Soler JM, Rubio A, Ordejón P. Phys Rev B 1999;59:12678–88.
[22] Jorio A, Souza Filho AG, Dresselhaus G, Dresselhaus MS, Saito R, Hafner JH, Lieber CM, Matinaga FM, Dantas MSS, Pimenta MA. Phys Rev B 2001;63:5416.
[23] Souza Filho AG, Jorio A, Hafner JH, Lieber CM, Saito R, Pimenta MA, Dresselhaus G, Dresselhaus MS. Phys Rev B 2001;63:1404R.
[24] Yu Z, Brus LE. J Phys Chem B 2001;105:6831–7.
[25] Brown SDM, Jorio A, Corio P, Dresselhaus MS, Dresselhaus G, Saito R, Kneipp K. Phys Rev B 2001;63:5414.
[26] Jorio A, Dresselhaus G, Dresselhaus MS, Souza M, Dantas MSS, Pimenta MA, Rao AM, Saito R, Liu C, Cheng HM. Phys Rev Lett 2000;85:2617–20.
[27] Saito R, Jorio A, Dresselhaus G, Dresselhaus MS. In: Ando T, editor, 25th International Conference on The Physics of Semiconductors, Osaka, 2000, p. 1629.
[28] Kahn D, Lu JP. Phys Rev B 1999;60:6535.
[29] Jorio A, Souza Filho AG, Brar VW, Swann AK, Ünlü MS, Goldberg BB, Righi A, Hafner JH, Lieber CM, Saito R, Dresselhaus G, Dresselhaus MS. Phys Rev B Rapid (2001) submitted.
[30] Duesberg GS, Loa I, Burghard M, Syassen K, Roth S. Phys Rev Lett 2000;85:5436–9.
[31] Kasuya A, Sasaki Y, Saito Y, Tohji K, Nishina Y. Phys Rev Lett 1997;78:4434.
[32] Tuinstra F, Koenig JL. J Chem Phys 1970;53:1126.
[33] Vidano RP, Fishbach DB, Willis LJ, Loehr TM. Solid State Commun 1981;39:341.
[34] Baranov AV, Bekhterev AN, Bobovich YS, Petrov VI. Opt Spectrosc USSR 1987;62:612.
[35] Matthews MJ, Pimenta MA, Dresselhaus G, Dresselhaus MS, Endo M. Phys Rev B 1999;59:R6585.
[36] Thomsen C, Reich S. Phys Rev Lett 2000;85:5214.
[37] Pocsik I, Hundhausen M, Koos M, Ley L. J Non-Cryst Solids 1998;227–230B:1083.
[38] Saito R, Jorio A, Souza Filho AG, Dresselhaus G, Dresselhaus MS, Pimenta MA. Phys Rev Lett (2002) submitted.
[39] Pimenta MA, Hanlon EB, Marucci A, Corio P, Brown SDM, Empedocles SA, Bawendi MG, Dresselhaus G, Dresselhaus MS. Braz J Phys 2000;30:423–7.
[40] Maultzsch J, Reich S, Thomsen C. Phys Rev B 2001;64:121407(R).
[41] Souza Filho AG, Jorio A, Dresselhaus G, Dresselhaus MS, Saito R, Swan AK, Ünlü MS, Goldberg BB, Hafner JH, Lieber CM, Pimenta MA. Phys Rev B (2001).
[42] Brown SDM, Jorio A, Dresselhaus G, Dresselhaus MS. Phys Rev 2001;B64:3403.
[43] Grüneis A, Hulman M, Kramberger Ch, Pichler T, Peterlik H, Kuzmany H, Kataura H, Achiba Y. In: Proceedings of the Int. Winter School on Electronic Properties of Novel Materials (IWEPNM'01), American Institute of Physics, Woodbury, 2002, in press.
[44] Woods LM, Mahan GD. Phys Rev B 2000;61:10651.